ASME Journal of Engineering for Gas Turbines and Power
Online journal at:
https://asmedigitalcollection.asme.org/gasturbinespower

Abdelrahman Abdeldayem[1]
Energy, Sustainability and
Net-zero Research Centre,
School of Science and Technology,
City, University of London,
London EC1V 0HB, UK
e-mail: abdelrahman.abdeldayem@city.ac.uk

Andrea Paggini
Baker Hughes,
Via Felice Matteucci,
Firenze 50127, Italy

Tommaso Diurno
Baker Hughes,
Via Felice Matteucci,
Firenze 50127, Italy

Claudio Orazi
Baker Hughes,
Via Felice Matteucci,
Firenze 50127, Italy

Martin White
Energy, Sustainability and
Net-zero Research Centre,
School of Science and Technology,
City, University of London,
London EC1V 0HB, UK;
Thermo-Fluid Mechanics Research Centre,
School of Engineering and Informatics,
University of Sussex,
Falmer, Brighton BN1 9RH, UK

Marco Ruggiero
Baker Hughes,
Via Felice Matteucci,
Firenze 50127, Italy

Abdulnaser Sayma
Energy, Sustainability and
Net-zero Research Centre,
School of Science and Technology,
City, University of London,
London EC1V 0HB, UK

Integrated Aerodynamic and Mechanical Design of a Large-Scale Axial Turbine Operating With A Supercritical Carbon Dioxide Mixture

In this paper, the design of a large-scale axial turbine operating with supercritical carbon dioxide (sCO_2) blended with sulfur dioxide (SO_2) is presented considering aerodynamic and mechanical design aspects as well as the integration of the whole turbine assembly. The turbine shaft power is 130 MW, designed for a 100 MW_e concentrated-solar power plant with turbine inlet conditions of 239.1 bar and 700 °C, total-to-static pressure ratio of 2.94, and mass-flow rate of 822 kg/s. The aerodynamic flow path, obtained in a previous study, is first summarized before the aerodynamic performance of the turbine is evaluated using both steady-state and unsteady three-dimensional numerical models. Whole-annulus unsteady simulations are performed for the last turbine stage and the exhaust section to assess the unsteady loads on the rotor due to downstream pressure field distortion and to assess the aerodynamic losses within the diffuser and exhaust section. The potential low engine order excitation at the last rotor stage natural frequency modes due to downstream pressure distortion is assessed. The design of the turbine assembly is constrained by current manufacturing capabilities and the properties of the proposed working fluid. High-level flow-path design parameters, such as pitch diameter and number of stages, are established considering a trade-off between weight and footprint, turbine efficiency, and rotordynamics. Rotordynamic stability is assessed considering the high fluid density and related cross coupling effects. Finally, shaft end sizing, cooling system design, and the integration of dry gas seals are discussed.
[DOI: 10.1115/1.4063530]

Keywords: axial turbine, sCO_2 mixtures, exhaust section, rotordynamics, thermal analysis, aeromechanical integration

1 Introduction

Supercritical carbon dioxide (sCO_2) power cycles are promising candidates for concentrated solar power (CSP) plants [1,2] where the compression process takes place in the supercritical region using a compressor. The SCARABEUS project [3], an EU-funded project, is investigating the applicability and potential benefits of transcritical power cycles operating with CO_2-mixtures to produce 100 MW_e, where the working fluid is compressed in the liquid phase. This could result in enhanced power generation efficiency and bring the levelized cost of electricity (LCoE) of CSP plants to a competitive level compared to other dispatchable power generation plants operating in a renewable-dominated energy market [4]. Several CO_2-based mixtures have been proposed to increase the mixture's critical temperature, and hence allow for ambient air

Turbomachinery Technical Conference & Exposition Hynes Convention Center June 26–30, 2023. Turbo Expo 2023.
[1]Corresponding author.
Manuscript received August 1, 2023; final manuscript received August 7, 2023; published online November 2, 2023. Editor: Jerzy T. Sawicki.

condensation using a transcritical power cycle in dry regions where water cooling is not available [3,5]. The CO_2–SO_2 mixture has been found to be promising to increase cycle thermal efficiency while offering good thermal stability for the operating turbine inlet temperature [6]. Morosini et al. [6] have shown that the adoption of CO_2–SO_2 mixture instead of pure CO_2 increases the cycle thermal efficiency by 2% using a recompression configuration. Considering the environmental hazards, the optimum cycle performance, and the thermal stability of the candidate mixtures at 700 °C, a molar mixture of 80% CO_2 and 20% SO_2 has been proposed with a predicted overall cycle thermal efficiency of 51% [7].

Numerous studies have been dedicated to the aerodynamic design of axial turbines [8–10]. However, a complete design considering the whole turbine design and integration aspects is less commonly found. The aerodynamic flow path and the design of the mechanical components, such as blade modal analysis, thermal analysis, and rotordynamic stability are highly coupled [11–13]. A typical turbine design process comprises aeromechanical integration at different stages. The flow path design is initiated subject to mechanical design constraints, such as stress limits and the rotor slenderness ratio [14]. The optimized flow path design is then used to inform decisions related to different mechanical components, such as cooling streams, casing design, and shaft arrangement [12]. The geometrical limitations on the casing design, rotor stability, and cooling system affect the exhaust section, which is aerodynamically optimized for performance subject to the given constraints. The exhaust section flow results are then used to quantify the alternating stresses on the blades, as well as the pressure fluctuations at the interface between the last stage and the diffuser inlet [15]. These fluctuations are used in the modal analysis, while the magnitude of the alternating stresses is used to assess the blade life and safety factor [16].

Several authors have presented the design of sCO_2 turbines at varying scales to reveal critical design considerations and the expected range of turbine efficiency. Zhang et al. [8] conducted a computational fluid dynamic (CFD) analysis of a 15 MW single-stage axial turbine and predicted a total-to-static efficiency of 83.96%. Additionally, they demonstrated the significance of gas bending stresses on the turbine blades. However, the potential benefits of adding additional stages to improve the turbine performance were not investigated. On the other hand, Shi et al. [9] predicted a total-to-total efficiency of 92.12% could be achieved with a three-stage design for a 10 MW_e axial turbine. Moreover, they showed that the turbine can maintain and efficiency between 85% and 92% while operating at off-design conditions with mass-flow rates in the range of 62.5% to 110% of the design value. Total-to-total efficiency above 90% was also predicted by Bidkar et al. [10] for a four-stage 50 MW_e and a six-stage 450 MW_e axial turbine, respectively. Kalra et al. [17] designed a four-stage axial turbine for a 10 MW CSP plant. The study focused on practical considerations such as mechanical integrity, vibrational damping, sealing, shaft assembly, and operational transients. It highlighted the unique challenges imposed by sCO_2 turbines, such as the high torque transmission requirements, small airfoil design and fabrication, aero-design optimization with mechanically safe blade design, and the high cycle fatigue life of the rotor. Wilkes et al. [18] presented the design, manufacture, and testing of a 10 MW sCO_2 turbine for CSP applications operating with turbine inlet conditions of 275 bar, and 700 °C. Thermal-structure interactions and fatigue analysis were presented for the expander casing. The results have shown that the design has successfully mitigated the risk of fatigue and creep while allowing for rapid thermal transients. Guédez et al. [19] discussed the conceptual design of a 2 MW sCO_2 power cycle, highlighting the proposed integration and operational regimes, expected thermodynamic performance at the nominal point, and up-scaling considerations. However, the performance of turbines operating with CO_2 mixtures, as well as the aero-mechanical design and integration has not been previously investigated.

The exhaust section in turbines is used to recover exit kinetic energy before the flow leaves the turbine. Numerous studies have investigated the effect of the exhaust section on the performance of steam turbines [20–22]. However, the exhaust section design generates a low engine order frequency that needs to be considered for the blade modal analysis [22]. The accuracy of prediction of the overall diffuser performance is strongly dependent on a proper coupling of both the rotor and exhaust domains. The most accurate, but most computationally expensive method, is an unsteady full annulus simulation [20]. The design of the exhaust section has been extensively studied for large-scale steam turbines, and the common exhaust section design is the radial type with an outbox. This type of exhaust section can cause pressure non-uniformity at the interface between the exhaust section and the last rotor domain, which has been shown to cause a low-frequency fluctuation in the aerodynamic force on the last stage rotor blades [15].

Numerous design challenges are introduced by the new working fluid proposed for the SCARABEUS project [3]. The high gas density leads to high bending stresses meaning the blade chord length is increased, and the number of blades per stage is decreased [23]. The mean line design optimization of the turbine has also revealed that a large number of stages are required to reach high design point efficiency under the given operating conditions [7,23]. Increasing the number of stages leads to a smaller hub diameter and longer blades, which introduces challenges related to the shaft lateral stability [24], and increased blade vibrations which is particularly important for the last rotor stage where the pressure fluctuations of the exhaust section are important. The optimized cycle operating conditions for the selected working fluids also lead to technical challenges related to the cooling system, exhaust hood design, and material selection considering manufacturability limitations.

In this paper, a comprehensive turbine design is presented for a 130 MW axial turbine operating with a CO_2/SO_2 mixture with an 80–20% molar composition. Both aerodynamic and mechanical design aspects, alongside integration considerations of the entire turbine assembly are investigated and discussed. General mechanical design considerations are first discussed, which is followed by a brief presentation of the flow path design and predicted aerodynamic performance. The turbine exhaust section design is then presented considering the integration with other mechanical design components. Following this, blade modal analysis, thermal analysis, rotor dynamic analysis, and torsional sizing analysis are presented for the proposed turbine design.

2 Mechanical Design Overview

The high-level considerations driving the conceptual mechanical design of the turbine are summarized in this section. The power delivered by the turbine (≈130 MW) is such that the direct drive arrangement with a two-pole synchronous generator is considered the only viable solution for this application. Although a geared design could be a feasible and convenient option for a smaller power rating (indicatively up to ≈50–60 MW), it can be discarded a priori for an application at such a high power rating based on practical experience.

Owing to the thermodynamic conditions at the inlet and outlet of the turbine, a barrel-type external casing is selected with the aim to

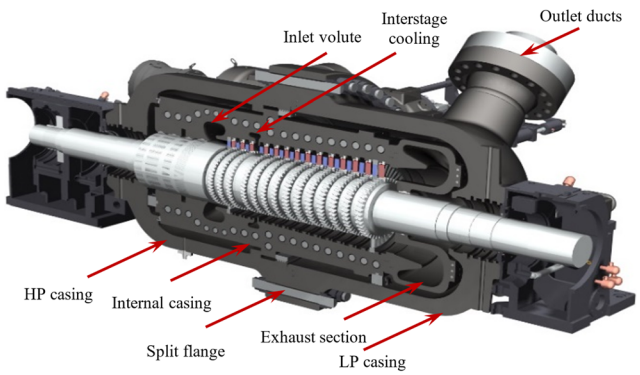

Fig. 1 Turbine assembly cross-section, Copyright 2023 by Baker Hughes Company—All rights reserved

minimize radial deformations. The design has a horizontal split of the casing, as shown in Fig. 1, separating it into high pressure (HP) and low pressure (LP) sides with a vertical split flange connecting the two sides. The inlet flow is admitted into an inner casing, accommodating all the stator blade rows, having a split plane containing the rotational axis of the machine. Machining and assembly constraints introduced the necessity of splitting the exhaust section, which is designed in a separate casing, into two halves.

Material compatibility with pure sCO_2 at high temperatures is presented in the literature [25]. However, no information is currently available about the compatibility with the working fluid used in this study. Industrial experience and supply chain considerations led to the decision to choose Ni-based alloys considering the high turbine inlet temperature and the poor characteristics of Martensitic steels, commonly used in ultrasupercritical steam turbines, with CO_2. Previous studies have shown that 12% of Cr martensitic steels are prone to high temperature oxidation and carburization when operated with CO_2. Considering the current limitations applied to manufacturing large castings and forgings in Ni-based alloys, it is decided to consider a limitation of approximately 20 tons for castings and 10 tons for forgings. Although these limits represent a stretch of the current references of the Baker Hughes suppliers, it was deemed that it is possible to obtain a quality of the raw materials in line with the standard acceptance criteria employed for castings and forgings.

Tests carried out within the Desolination project have the goal of providing high level indications about the compatibility of materials with the process fluid at high temperatures [26]. The tests are aimed at identifying the alloys experiencing no or minimal interaction with the fluid as promising materials in view of practical industrial applications. A testing campaign is ongoing to have a thorough material assessment by characterizing the tensile and fatigue properties after a long exposure time.

The main design input that can be varied in the conceptual design phase is the rotor hub diameter as the rotational speed is fixed at 50 Hz. Whilst the aerodynamic design parameters, such as the loading coefficient, flow coefficient, degree of reaction, and blade solidity can be optimized, the choice of the hub diameter has the most significant influence. For a small hub diameter, the flow path tends to have more stages, since the peripheral speeds of the stages are low, and the ratio between tip and hub radii is generally increased. Having a flow path with a small hub diameter is beneficial to limit the weight of the main components (rotor, inner casing, and external casings), in line with the current manufacturing constraints. It is also beneficial for the torsional dimensioning of the rotor shaft ends as explained in Sec. 5.5.

Considering the hub diameter, dry gas seals (DGS) are selected to limit the leakage flows in view of a life cycle assessment [27,28]. Considering the limitations of the DGS technology, the shaft end diameter is in the order of 350–400 mm. The shaft end sizing is driven by the need to withstand the electrical malfunctioning torques such as short circuit and out-of-phase synchronization, rather than the normal operating torque. More details are given in Sec. 5.5 about the torsional sizing. The smaller hub diameter results in a higher blade radius ratio, and hence interstage leakages have less impact on the turbine performance and the aspect ratio of the airfoils is more favorable. It is found that the hub diameter reduction encounters rotor-dynamic stability limitations as well; these aspects are discussed in Secs. 5.2 and 5.4.

Cooling streams are designed for the turbine casings so that the necessity for using Ni-based alloys is avoided to satisfy the current manufacturing limitations. Alternatively, 12% Cr stainless steel can be used for the external casings while Ni-based alloys are used for the rotor shaft, blades, inner casings, and trip & throttle valves. A cooling stream is designed at around 450 °C as described in Sec. 5.3, to limit the oxidation and carburization of 12% Cr Martensitic steel in a pure CO_2 environment [25]. However, it is yet to be ascertained whether this temperature is acceptable in case of working fluid containing SO_2.

The dry gas seals are among the most critical components for the turbine mechanical design. The installation of these seals in sCO_2 turbines is challenged by the high pressure, high temperature, and high speed. These conditions lead to high thermal loads on the seal which significantly over complicates the design. The maximum allowable temperature by the DGS is limited to 220 °C which requires the employment of an additional cooling stream (at around 160 °C) for the shaft end zones. In this regard, a dedicated thermal management system has been designed considering the findings proposed by the authors in another publication in which a segregated conjugate heat transfer numerical procedure has been presented and validated with experimental data provided by FLOWSERVE with a rotating DGS test bench in sCO_2 environment [29,30].

The material cooling requirements, along with the manufacturing capabilities, limit the design space for the aerodynamic optimization of the exhaust section. Moreover, the geometry of the exhaust section is intrinsically prone to generating circumferential pressure nonuniformities downstream of the last stage, which could pose concerns for the mechanical design of the last rotor stage. The exhaust section optimization and the impact on the last rotor stage are analyzed in Secs. 5.1 and 5.2.

3 Numerical Model Description

Numerous three-dimensional (3D) viscous CFD models are setup to simulate the aerodynamic performance of the proposed 14-stage turbine and the exhaust section. Firstly, a single passage steady-state CFD model of the 14 stages is setup to verify the mean line design results of the flow path and generate the turbine aerodynamic performance maps. Then, three different CFD models are setup including the exhaust section to select the best geometry, study its effect on the entire turbine, and study its effect on the last stage, respectively. The first model is steady-state simulating the exhaust section in isolation to assess the aerodynamic performance of a given cross-section geometry. The second model is a steady-state single passage multistage CFD model simulating the interaction between the 14 stages and the exhaust section to quantify the effect of the exhaust section on the entire turbine performance. The third model is used to study the steady-state and unsteady circumferential variations caused by the exhaust section geometry on the last turbine stage. In the third model, a full annulus of all stator and rotor blades in the last stage is modelled along with the exhaust section as seen in Fig. 2. The boundary conditions of the reference 14-stage model, as well as the three models dealing with the exhaust section, are summarized in Table 1.

The CFD models are Reynolds averaged Navier–Stokes simulations and use the shear stress transport (k–ω SST) turbulence model as it has been found the most suitable model for turbomachinery applications [31]. In the steady-state models, the interface between the stator and rotor domains is treated as a mixing plane which has been proven to give high-quality results with the least numerical instabilities compared to the frozen rotor approach [32]. However, the interface between the last rotor blade and the exhaust inlet is a frozen rotor to consider the circumferential variations caused by the exhaust section geometry. All the interfaces in the unsteady model are sliding plane interfaces. The rotor is shrouded with a clearance gap between the shroud and the casing

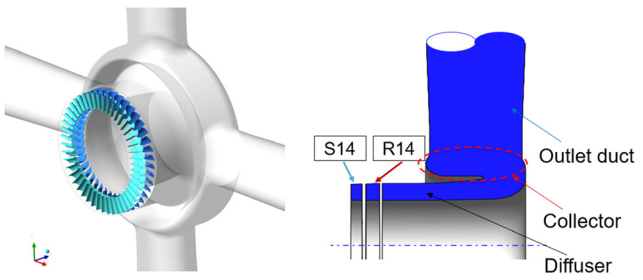

Fig. 2 Geometry definition of model 3: the full annulus of the last turbine stage along side with the exhaust section cross-section

Table 1 Boundary and operating conditions of the proposed numerical models

Parameter	Reference	Model 1	Model 2	Model 3
Type	Steady	Steady	Steady	Steady + unsteady
Geometry	14 Stage (single)	Exhaust (E)	14 Stage (single) + E	Last stage (Full) + E
Inlet total pressure (bar)	239	—	239	—
Inlet total temperature (K)	973.15	829.0	973.15	839.2
Inlet mass flow rate (kg/s)	—	822	—	822
Outlet static pressure (bar)	81.24	81.24	81.24	81.24

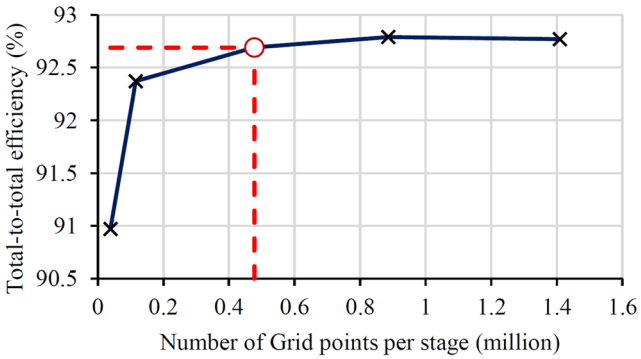

Fig. 3 Mesh sensitivity analysis of the 14-stage reference model

0.07% of the tip diameter for each stage. The rotational speed is fixed at 3000 RPM (50 Hz).

The thermophysical properties of the working fluid are evaluated using the Peng Robinson equation of state [6,33] and the properties are introduced to the model through look-up tables generated to cover the expected pressure and temperature ranges with a resolution of 500 × 500 points.

The unsteady simulation is setup in two models; the first model is initiated from the steady-state solution and advances over time for three complete rotor revolutions where $t_{rev} = 0.02s$ with a course time-step of $t_{blade}/20$ to correct the initial steady-state solution and provide a more accurate transient performance for the detailed analysis. The blade passing time is calculated from $t_{blade} = t_{rev}/N_{R14}$ where N_{R14} is the 14th rotor number of blades = 42. This time-step is selected based on an iterative approach starting from five steps per blade pass while the obtained performance is found almost the same after 20 steps per blade pass. The second model is initiated from the last time-step obtained from the first model and advances over time for 1 complete revolution with a finer time-step of $t_{blade}/200$ to accurately predict the blade load variations over time relative to a blade's relative position between the stator blades and the exhaust section outlet ports.

The meshing structure of the flow path is generated using TURBOGRID solver built into ANSYS software version 2020R2. The sensitivity of the total-to-total efficiency to the average number of grid points per stage is reported in Fig. 3 where it can be seen that 475 k grid points are required to achieve a tolerance relative to the finest mesh of 0.1%. The average number of grid points in the stator, and rotor blades is around 190 k, and 285 k, respectively. This difference is normally due to the tip clearance gap considered in the rotor domains.

The mesh of the entire geometry is adjusted to achieve y^+ values between 30 and 100 where the wall functions are best suited. The mesh structure of the exhaust section is completed using the ANSYS mesh solver where the elements size is controlled considering a mesh-independent entropy rise across the exhaust section and a symmetric pressure distribution on the exhaust section walls as reported in Fig. 4. The mesh of the exhaust section is defined by 1.2×10^6 grid points. The uncertainty of the exhaust section model calculated from the entropy rise values contributes to the entire turbine assembly by around 0.03%.

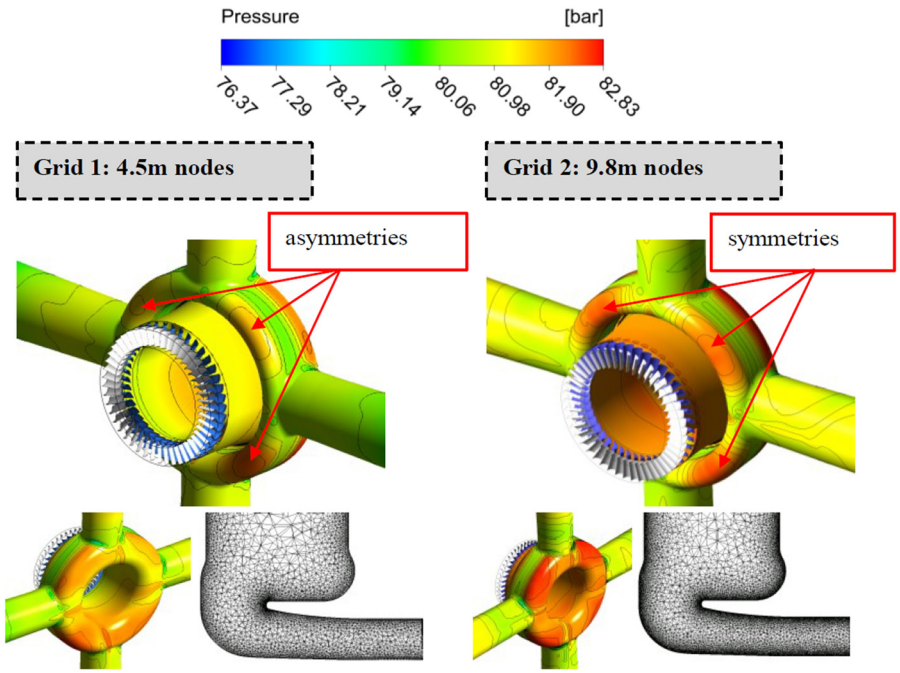

Fig. 4 Effect of grid structure on the pressure distribution patterns obtained on the exhaust section walls

Table 2 Comparison between the flow path design using different number of stages

Parameter	Four-stage model	Nine-stage model	14-stage model
Hub diameter (m)	1.21	0.81	0.62
Flow path length (m)	0.52	1.0	1.8
Inlet Mach number	0.46	0.31	0.25
Total-to-total efficiency at the design point (%)	85.86	92.11	92.81
Total-to-total efficiency at 50% mass flow rate (%)	72.38	78.12	80.69
Minimum mass flow ratio to the design point, $\eta_{tt} > 70\%$	0.480	0.437	0.418

Furthermore, a 3D finite element analysis (FEA) model is setup for the full rotor blades of the last stage to quantify the alternating stresses resulting from the exhaust section geometry. The aerodynamic loads (i.e., pressure distribution over the blade surfaces) predicted within the CFD simulations are transferred to the FEA model, along with the centrifugal load on the rotor blades due to rotation. The blades are fixed at the base of a 10 mm thick plate representing the hub surface with a fillet modeled between the blade and the base to introduce manufacturing allowance and to avoid any numerically generated stress peaks at the sharp corner. For the FEA analysis, nickel-based alloys potentially represent a good choice for the blades as they are commonly used with gas turbine blades that can operate at temperatures up to 1000 °C whilst maintaining a high yield strength suitable for the proposed operating conditions [34].

Both CFD and FEA models have been verified against a published numerical study of a sCO_2 turbine in the authors' previous work [35].

4 Turbine Flow Path Design

The turbine blades are generated using the mean line results to create an initial geometry to initiate the numerical analysis. Numerous design criteria are introduced to account for the various mechanical design limitations such as bending stress, and slenderness ratio [35,36]. Design iterations made using the mean line design model revealed that the total-to-total efficiency can be increased by increasing the number of stages and decreasing the hub diameter as reported in Table 2. Increasing the number of stages from 4 to 14 results in an increase in total-to-total efficiency of 6.9%, thus achieving a design total-to-total efficiency of 92.8% due to the reduction in peripheral speed from 194 to 107 m/s, and hub diameter reduction from 1.2 to 0.62 m. Increasing the number of stages beyond 14 stages marginally increases the total-to-total efficiency while the increase in slenderness ratio may have a negative impact on the rotor stability.

The off-design performance of the proposed models is investigated using the 3D numerical model and added to the comparison in Table 2. It is found that the 14-stage design has better turndown capability as it can run down to 41.8% of the design mass flow rate with an acceptable efficiency of over 70% compared to 48.0% and 43.7% for the four-stage and nine-stage designs, respectively. The efficiency gain by selecting the 14-stage design at half load is calculated at 8.31%, and 2.57% compared to the four-stage, and nine-stage models, respectively.

A 3D numerical CFD model is setup to verify the mean line design and initialize the 3D blade shape optimization. The blade geometry is initiated using the one-dimensional mean line design parameters in addition to some geometrical assumptions which are optimized in a subsequent design stage to give the best possible performance. Untwisted turbine blades are assumed due to the small blade height to mean diameter ratio of 11.5%, on average. The key design parameters are reported in Table 2, where it can be seen that the CFD predicts a 92.8% total-to-total efficiency and a total power production of 132 MW power, as required for a 100 MW_e power cycle for a CSP plant [3]. It is worth mentioning here that the total-to-total efficiency is obtained for the flow path excluding any leakage flow streams except for the rotor tip leakage.

The turbine performance is further improved by blade shape optimization as explained in the author's previous work [35], where the applied constraints limit the maximum allowable equivalent stress to 400 MPa and the mass flow rate to 2% of the cycle design mass flow rate. The blade optimization challenges are mainly due to the number of decision variables that can fully represent the profile shape. In addition, the high working fluid density have increased the blade loading and the mass flow rate sensitivity to the blade profile geometry. In this case, the optimization objective is more restricted to satisfy the system constraints rather than achieving a better aerodynamic performance.

A comparison between the reference and optimized blades has shown an increase in the total-to-total efficiency from 90.2% obtained from the initial blade model to 92.8% for the optimized geometry. The optimized geometry for the first stage showed only slight variations when compared to the last stage. This is because turbulence is much lower at the turbine inlet compared to the cumulative turbulence effects at the final stages. As a result, the inlet wedge angle is significantly increased in the last stage from 15 deg to 26 deg to account for the larger flow angle deviation from the blade angle and limit the flow separation.

5 Results and Discussion

After the flow path design phase is completed and the 3D blades are finalized, the complementary design aspects are initiated. These include the exhaust section design, the blades modal analysis, thermal analysis, rotordynamic analysis, and shaft torsional sizing.

5.1 Exhaust Section Aerodynamic Performance. Exhaust sections are normally used in axial turbines to recover part of the kinetic energy into power output with the least possible aerodynamic losses. Due to space limitations driven by the design of the cooling system and by rotor-dynamic constraints, a new exhaust section is proposed instead of the commonly used radial exhaust with outlet box, that is typically used in large-scale steam turbines, as illustrated in Fig. 1 of the proposed exhaust section integrated within the turbine assembly, and Fig. 2 of the numerical domain. The reference diffuser and collector cross-section geometry has been designed between 580:1310 mm radial location, and 1680:2250 mm axial location with an area ratio of 1.17 for the diffuser part. Different geometry cross-sections and numbers of outlet ducts have been iterated to achieve the best aerodynamic performance whilst considering mechanical constraints. The reference cross-section is designed as an initial guess aiming at utilizing the available space and making the diffuser section as long as possible. Numerous modifications are tested while the selected cross-sections are M_1, M_2, and M_3. M_1 is designed to increase the diffuser area ratio while keeping the sharp turn between the diffuser and collector. M_2 is modified by decreasing the diffuser length to facilitate the flow turn between the diffuser and collector while the diffuser section is almost removed in the M_3 section to further improve the flow turn. The modified diffuser and collector cross-sections relative to the reference cross-section are summarized in Fig. 5.

A set of numerical models are setup for the different cross-sections as defined in Table 1 with two and four outlet ducts. The expansion enthalpy-entropy diagram is plotted for the different models as reported in Fig. 6 where E_2 and E_4 correspond to two and four outlet ducts, respectively, and the R, M_1, M_2, and M_3 are the reference, modifications 1, 2, and 3 cross-sections, respectively. In

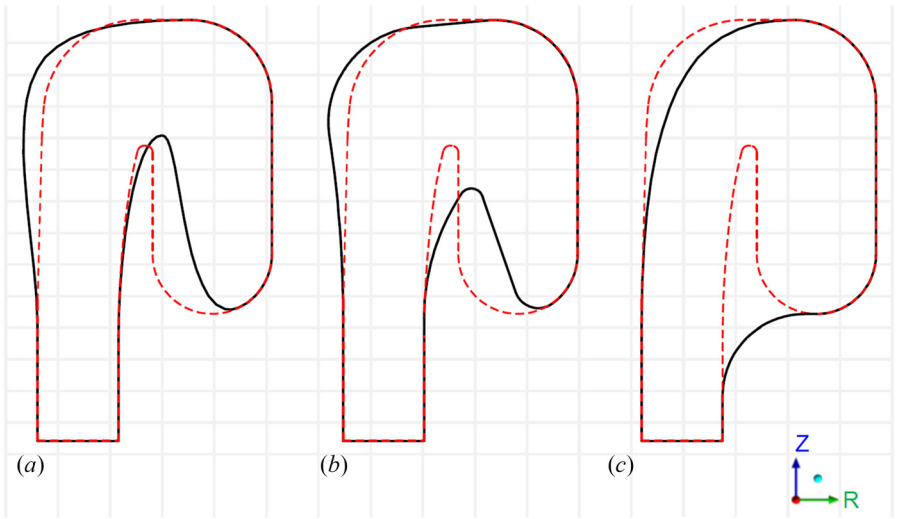

Fig. 5 Modified diffuser and collector cross-sections relative to the reference cross-section: (*a*) M_1, (*b*) M_2, and (*c*) M_3

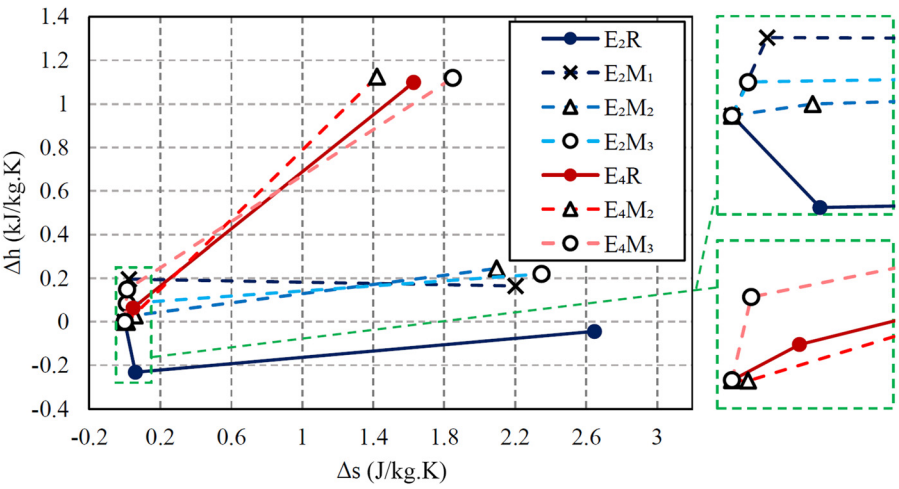

Fig. 6 Enthalpy-entropy diagram of the different exhaust geometries. Different cross-section and different numbers of outlet ducts. Left: full data, and right: zoom in view.

the figure, each curve is represented by three points where the first and second points are for the diffuser inlet and outlet while the endpoint is the outlet from the exhaust ducts. As can be seen from the figure, the two outlet designs (E_2) experience higher total entropy rise due to the long circumferential distance between the outlet ports which increases the distance a flow needs to travel until reaching the outlet. For the E_2 models, the outlet kinetic energy is still high because of the limited outlet cross-sectional area. By comparing the different cross-sections, it can be seen that the M_2 design achieves the lowest entropy rise and hence the best aerodynamic performance with both E_2 and E_4 options.

Furthermore, the breakdown of the entropy rise is investigated as shown in Fig. 7. It is noted that the losses in the diffuser section are almost negligible while the collector and outlet ducts dominate the performance. The E_4M_2 design corresponds to the lowest total losses with the lowest amount of entropy rise in the outlet ports. By comparing the E_2 and E_4 designs, it can be seen that the collector losses are higher in the E_2 design as discussed. By comparing the M_3 and the M_2 cross-sections, the M_3 geometry has minimum flow restrictions in the collector domain, designed to give better aerodynamic performance, however, this design records higher total losses. Although the M3 design has achieved lower collector losses, the losses in the outlet ducts are the highest as the flow toward the ducts is unguided and generates more losses. The total entropy rise, loss in total pressure, and change of kinetic energy across the exhaust section are summarized and compared in Table 3 where the results agree with the observations made from Figs. 6 and 7. It can be

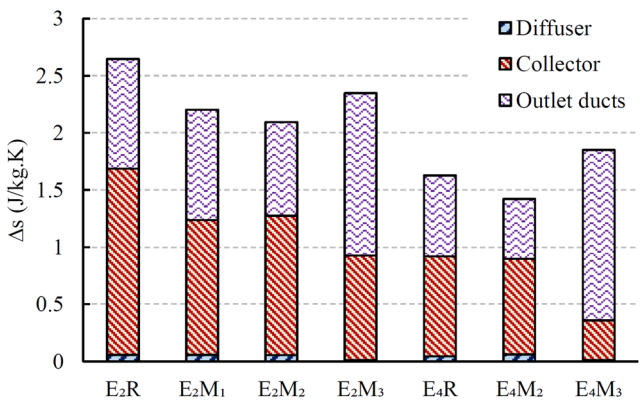

Fig. 7 Loss breakdown analysis of the different exhaust section geometries

Table 3 Comparison between the performance of the different exhaust section geometries

Model	E_2R	E_2M_1	E_2M_2	E_2M_3	E_4R	E_4M_2	E_4M_3
Δs_{total} (J/kg K)	2.65	2.20	**2.10**	2.35	1.63	**1.42**	1.85
$\Delta P0_{total}$ (bar)	–1.25	–1.05	**–0.98**	–1.11	–0.76	**–0.66**	–0.85
C_{out} (m/s)	52.8	48.9	**47.9**	47.9	24.9	**24.4**	25.0
C_{in} (m/s)	52.4	52.6	**52.7**	52.6	53.1	**53.2**	53.1
$\Delta K.E$ (kJ/kg)	0.02	–0.19	**–0.24**	–0.24	–1.10	**–1.12**	–1.10

Note: The cross-section resulting in the minimum losses for each number of outlet ducts is highlighted in bold.

noted from the table that increasing the number of outlet ducts from 2 to 4 using the M2 cross-section decreases the entropy rise across the exhaust section by 32%. By comparing the entropy rise across the exhaust section to the entropy rise across the 14-stages which is calculated around 14.8 J/kg K, it can be calculated that increasing the number of outlet ducts to 4 decreases the overall turbine losses by around 4%.

The flow field of the different cross-sections is further analysed in Fig. 8 for the reference cross-section and Fig. 9 for the three proposed modifications. The diffuser section of the reference design (E_2R) is found to accelerate the flow instead of diffusing it due to the flow pattern which creates an effective flow area ratio less than 1 as shown in Fig. 8. The large counter-rotating vortex at the end of the collector section of the reference design increases the losses. The size of this vortex is decreased significantly in the first two modifications (M_1, M_2) and completely avoided in the third modification (M_3). By investigating the collector section, it has been found that the M3 design shows the lowest collector losses; however, this design didn't give the best overall exhaust section performance. The best combination of collector and outlet duct losses is found with the M_2 cross-section and four outlet ducts. Thus, this geometry is selected for the final turbine design.

The aerodynamic interaction between the turbine stages and the exhaust section is studied by solving a single passage 14-stage CFD model with the exhaust section for the reference and M_2 models. The change in the power produced per stage is calculated for the two models with respect to the reference 14-stage model without an exhaust section and the results are plotted in Fig. 10. Although the exhaust sections in turbines are designed to recover pressure and increase the power output, the power produced from the proposed turbine is slightly reduced because of the special geometrical limitations on the proposed exhaust section which increased the aerodynamic losses. In the meanwhile, the design kinetic energy at the last stage outlet is not sufficiently high to compensate for the generated aerodynamic losses and produce a positive pressure recovery. As seen in the figure, the last stage is the most affected by the exhaust section with a drop of around 2% of the reference value for the M_2 model. This effect is found to decrease in the upstream stages with a change in power production of less than 0.1% for the first stage in the M_2 model. By comparing the reference and modified cross-section geometries of the exhaust section, it appears that the reference geometry causes a larger power drop due to the higher losses experienced as explained in Table 3.

The results of the 14-stage model with and without the exhaust section are summarized in Table 4 which has shown a slight increase in the total-to-total efficiency obtained using the E_4M_2 exhaust section due to the achieved pressure recovery. The power produced by the whole turbine as well as the mass flow rate with and without the exhaust section is almost the same.

Although the effect of the exhaust section on the aerodynamic performance of the whole turbine is not significant, the potential forced excitation, which might be detrimental to the rotor blade dynamic behavior, needs to be investigated. These excitations are expected due to the number of outlet ducts which affects the pressure distribution downstream of the last rotor stage. The full annulus of the last stator and rotor blades are modeled with the exhaust section, as explained in Fig. 2, while both steady and unsteady performance are evaluated.

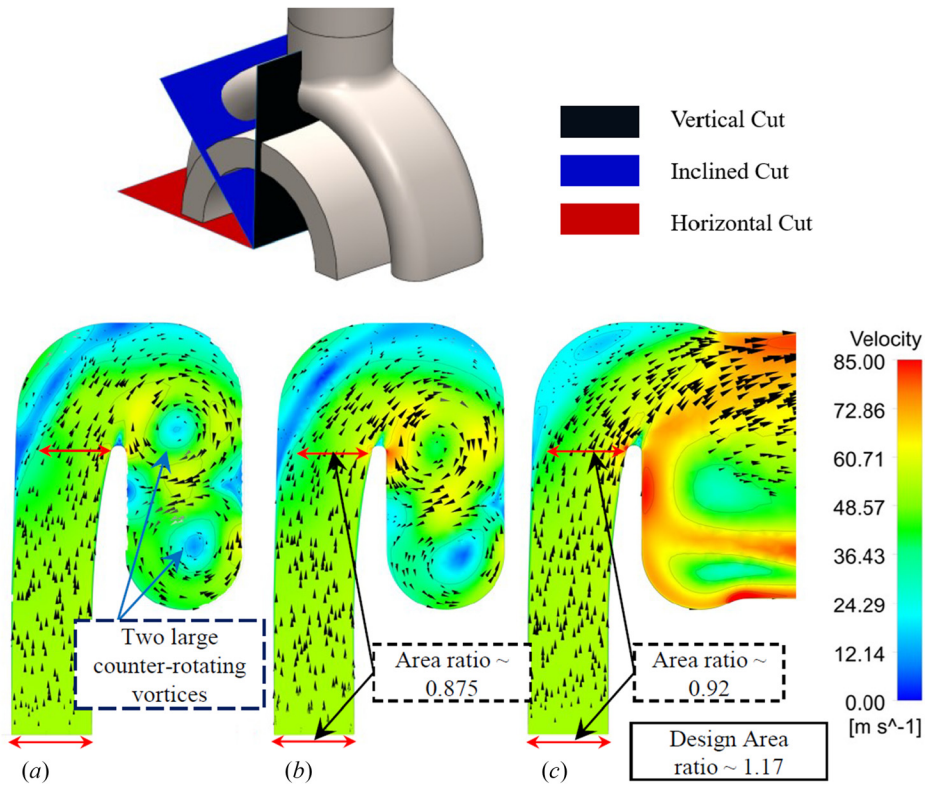

Fig. 8 Flow field in the reference diffuser and collector cross-section at (*a*) horizontal cut, (*b*) inclined cut, and (*c*) vertical cut

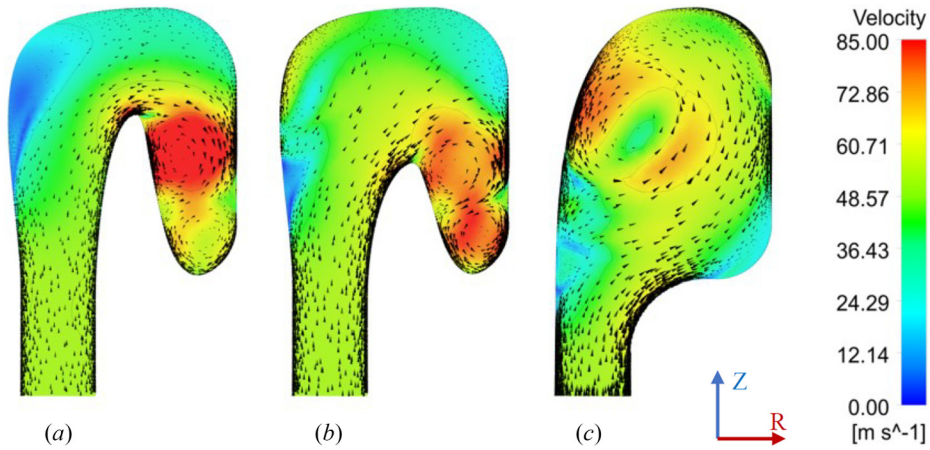

Fig. 9 Flow field obtained in the different cross-section modifications at an inclined cut midway between the periodic plane and the centre of the outlet duct: (*a*) M_1, (*b*) M_2, and (*c*) M_3

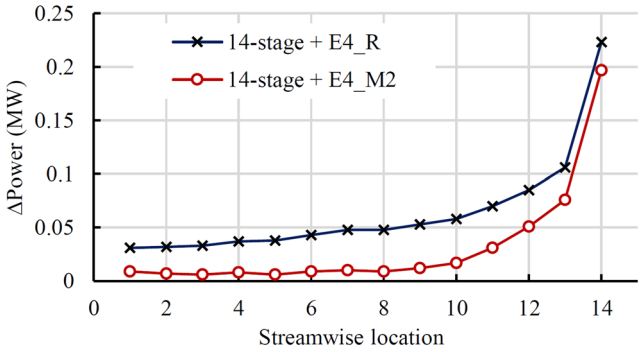

Fig. 10 The drop in power produced per stage with respect to the reference 14-stage model without the exhaust section

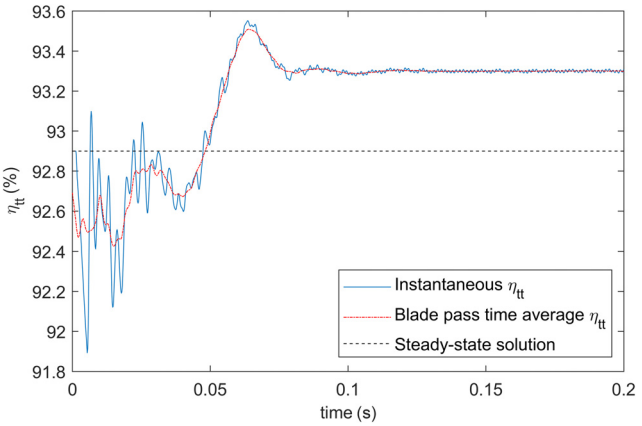

Fig. 11 Unsteady variation of the total-to-total efficiency of the last stage compared to the steady-state solution

Table 4 Comparing the performance of the 14-stages with and without the exhaust section for the *R* and M_2 cross-sections

Model	14-stage	14-stage + E_4R	14-stage + E_4M_2
$\dot{m}$ (kg/s)	822.892	822.062	822.646
Power (MW)	130.103	129.198	129.655
η_{tt} (%)	92.89	92.82	92.98

Table 5 Comparing the performance of the reference and modified exhaust sections obtained from the full annulus model

	SRE E_4R (steady)		*SRE* E_4M_2 (steady)		*SRE* E_4M_2 (unsteady)	
Model	*SR*	*E*	*SR*	*E*	*SR*	*E*
ΔP_0 (bar)	7.56	1.57	7.56	1.27	7.50	1.27
Δs (J/kg K)	0.79	3.44	0.79	2.74	0.89	2.78
ΔP (bar)	7.62	0.86	7.66	0.53	7.53	0.59
C_{exit} (m/s)	55.80	24.70	56.06	24.74	55.78	24.09
Power (MW)	9.86	—	9.95	—	9.79	—

(*SR*) stands for the last turbine stage, and (*E*) stands for the exhaust section.

A comparison between the steady-state and the time-averaged unsteady performance of the last stage (SR) and the exhaust section (*E*) is reported in Table 5. The comparison between the steady M_2 and *R* models confirms the previous observations where the loss in total pressure and entropy rise across the exhaust section are higher in the reference model. By comparing the steady and unsteady performance of the M_2 model, it can be seen that the unsteady losses are slightly higher as the entropy rises across the stage and the exhaust domain are both higher However, the drop in total pressure is around 0.8% lower in the unsteady model and the power produced is less by 1.6%.

The unsteady variation of the total-to-total efficiency of the last turbine stage full annulus model is shown in Fig. 11. The time shown in the figure corresponds to 10 complete rotor revolutions as the revolution time is 0.02 s. Convergence has been achieved after around five complete revolutions while the difference between the steady-state and unsteady solution is found within 0.4%. After five revolutions, the total-to-total efficiency value keeps oscillating within 0.02% which defines the unsteady model uncertainty.

The steady-state fluctuation of aerodynamic force magnitudes on a rotor blade of the last stage is presented in Fig. 12 along with the corresponding maximum equivalent stresses obtained using FEA analysis of the blade. In the figure, the normalized rotor circumferential position is the blade angular position divided by 360 deg. It can be seen that the steady-state model does not accurately predict the peaks corresponding to the number of outlet ducts as the force magnitudes are not only dependent on the rotor blade position relative to the outlet ports but also the relative position corresponding to the upstream stator blades which cannot be predicted using the stage mixing plane interface.

A more accurate prediction can be obtained using the sliding plane interface between the stator/rotor and the rotor/exhaust in the unsteady model. The unsteady model is initiated using the steady-state solution and advanced in time for three complete revolutions

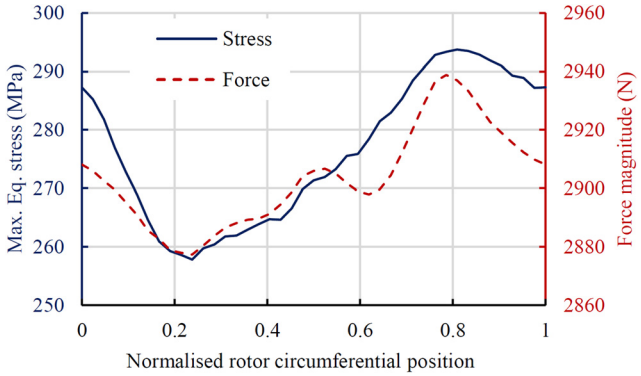

Fig. 12 Aerodynamic force magnitudes on the last rotor blades along the circumferential direction as obtained from the steady-state model

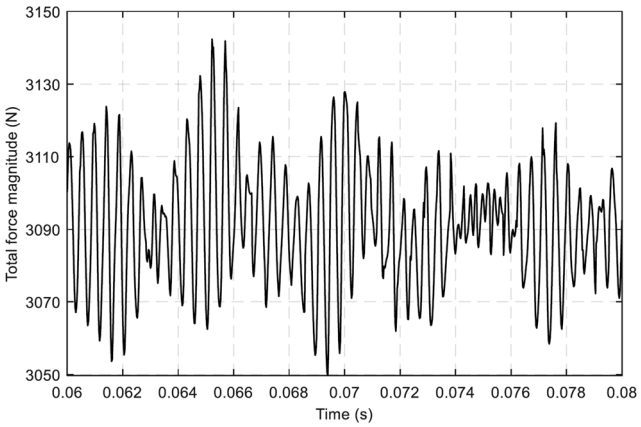

Fig. 13 Total force magnitude fluctuation on the last rotor blades over time for one complete rotor revolution

until the fluctuation in inlet total pressure and the entropy rise across the exhaust section are periodic. The results of the unsteady force fluctuation on the last stage rotor blades are given in Fig. 13 for one complete revolution starting after three revolutions of the first model. The results show variations between 3050 N and 3143 N compared to 2877 N and 2939 N obtained using the steady-state model with around a 6.1% difference in the mean value. The variation in the maximum equivalent stresses is evaluated using both models and applied to the Goodman diagram reported in the following section.

The force fluctuation in the time domain is converted into the frequency domain, as reported in Fig. 14, to evaluate and compare the strength of the dominant frequencies. A strong effect of the frequency corresponding to four times the rotational frequency (4xREV) is observed compared to the main frequencies, 42xREV and 47xREV, corresponding to the number of rotor and stator blades, respectively. However, frequencies corresponding to the number of stator and rotor blades of that stage are stronger. The figure has shown that the frequency corresponding to the number of outlet ports decreases significantly starting from the 8xREV frequency which is cut to 74% compared to the 4xREV frequency. More details about the blade mechanical analysis are given in Sec. 5.2.

5.2 Blade Mechanical Analysis. The design chosen for the rotating blades is with a firtree root and integral shroud. The firtree geometry allows a radial dimension of the root that is much smaller compared to a simpler T-root design, which would have been feasible due to the low peripheral speed of the final flow path selected (106 m/s for the first stage and 116 m/s for the last one); this

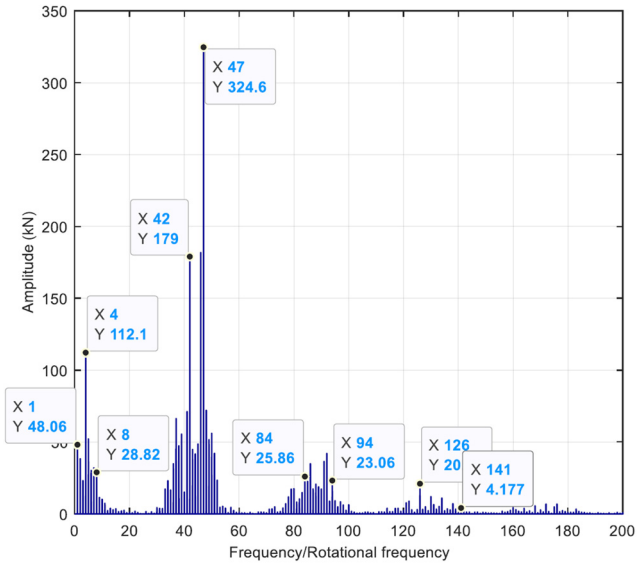

Fig. 14 Frequency domain of the blade force wave given in Fig. 13

choice results in a larger stiffness diameter of the rotor in the flow path region which is beneficial for the rotor-dynamic stability.

The chords of the airfoils, selected preliminarily targeting static stresses acceptable for the creep limit of the material, have been found to also produce an acceptable design from a dynamic point of view. The natural frequencies are sufficiently spaced away from the potential excitations as can be seen in the Singh's advanced frequency evaluation (SAFE) diagrams of the first and last rotor stages (Figs. 15 and 16). Moreover, despite the absence of critical resonances, it has been confirmed that, for the last rotor stage, the alternate stresses generated by the nonuniform circumferential distribution of the pressure downstream of the last stage are acceptable in terms of high cycle fatigue. Fig. 17 reports the Goodman diagram of the stage in dimensionless form.

Nickel-based alloys represent a good choice for the blades because of their good mechanical properties (primarily creep and high cycle fatigue). As already remarked, the compatibility with the process fluid is yet to be ascertained. The geometrical characteristics of the first and 14th stages as well as the Young's modulus are reported in Table 6.

Although the application is at a fixed speed of 3000 RPM, the SAFE diagram reports the harmonics of 95% speed and 105% speed to ensure that no critical encroaches are present in the vicinity of the synchronous speed. The potential sources of excitation considered are the nozzle passing frequency (1xNPF), 2xNPF, low harmonics of the rotating speed (up to 15xREV), (number of upstream blades – number of blades), and (number of downstream blades – number of blades).

Concerning the first stage, shown in Fig. 15, it is observed that no encroaches are present either with 1xNPF or with 2xNPF. The potential excitations (number of upstream blades – number of blades), and (number of downstream blades – number of blades) are not critical, since they do not encroach any natural mode of the stage. The first encroach with the harmonics of the rotating speed (with the additional margin ± 5%) is with the 47th mode, which is a very high harmonic order, and not critical for the mechanical design of the stage.

Concerning the 14th stage presented in Fig. 16, it is observed that the 1xNPF is not encroaching on any natural modes of the stage whereas 2xNPF has a 5% margin with respect to the third mode which, nonetheless, is the minimum separation margin acceptable. The potential excitation (number of upstream blades – number of blades) is not critical, since it does not encroach any natural mode of the stage. The first encroach with the harmonics of the rotating speed (with the additional margin ± 5%) is with the 35th mode, which is a

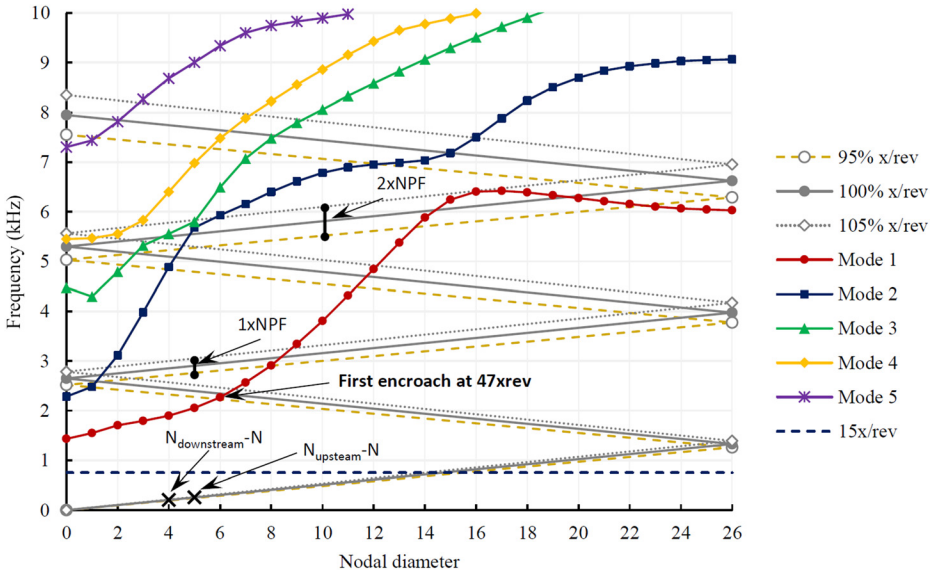

Fig. 15 SAFE diagram of the first rotor stage, Copyright 2023 by Baker Hughes Company—All rights reserved

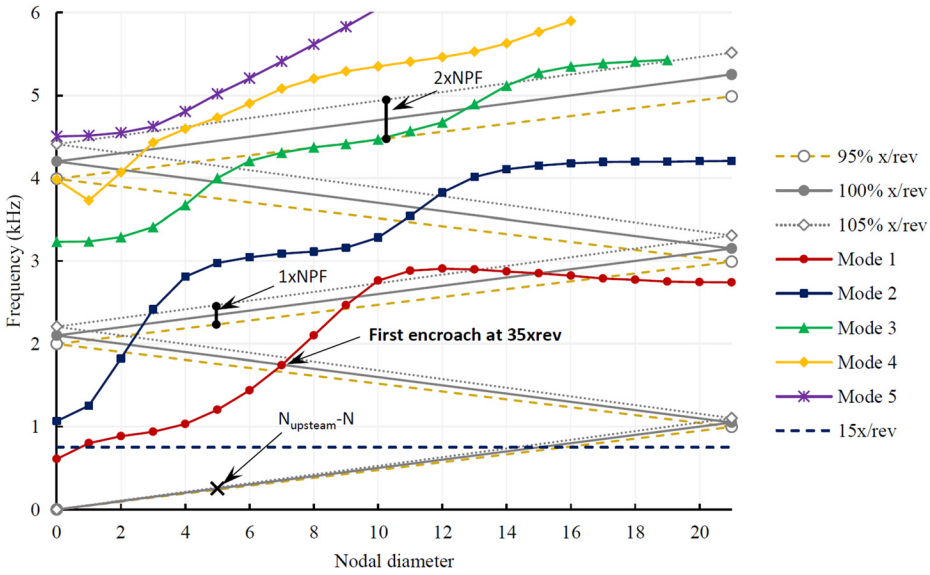

Fig. 16 SAFE diagram of the 14th rotor stage, Copyright 2023 by Baker Hughes Company—All rights reserved

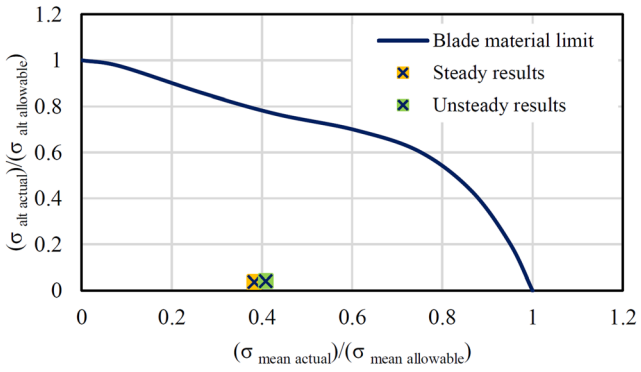

Fig. 17 Dimensionless Goodman diagram for the last rotor stage, Copyright 2023 by Baker Hughes Company—All rights reserved

very high harmonic order, and not critical for the mechanical design of the stage.

The maximum equivalent stresses fluctuations of the last stage rotor blades, obtained using both steady and unsteady CFD calculations, are located on the Goodman diagram, as shown in Fig. 17. It can be seen that the alternate excitations are largely within the high cycle fatigue capability of the blade material.

Table 6 The geometries of the first and 14th stages

Stage	First stage	14th stage
Hub diameter (mm)	620	620
Blade height (mm)	28.7	59.2
No. of vanes upstream	58	47
No. of buckets	53	42
No. of vanes downstream	57	—
Young's modulus (MPa)	164	174

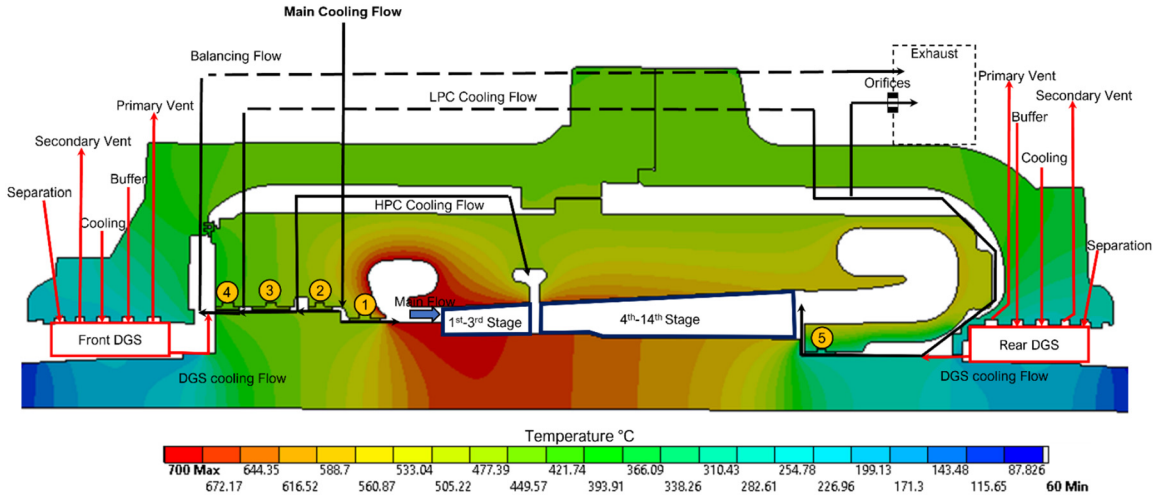

Fig. 18 Secondary flow scheme and thermal map, Copyright 2023 by Baker Hughes Company—All rights reserved

5.3 Thermal Analysis. Due to the high inlet temperature of 700 °C, an external cooling flow is utilized to cool both the rotor balancing piston and the external casing. In this case, 12% Cr steel material can be used for the external casing, avoiding the need for superalloys. A schematic representation of the cooling flows is reported in Fig. 18 together with the thermal field obtained with a two-dimensional axisymmetric model of the expander. This cooling system has been designed with the commercial fluid network solver "Altair flow simulator," which iteratively solves the conservation of mass, momentum, angular momentum, and energy, giving a punctual set of results in terms of pressure, temperature, swirl, and mass flow rate.

The cooling flow (2.2% of the expander exhaust flow) is injected into the internal casing (main cooling flow) and is over-pressurized compared to the expander inlet pressure. The cooling flow is split into two streams; a small stream flows to the right through seal n°1 which is reintegrated into the main flow path while the larger cooling flow stream is directed toward the balancing chamber through seal n° 2. The mass flow distribution is controlled by the number of teeth of the seals resulting from a sensitivity analysis aiming primarily at minimizing the total cooling flow for a fixed pressure drop to limit the impact on the cycle thermal efficiency. The teeth distribution of seals N° 2, 3, and 4 are optimized to provide the proper cooling flow for the casing chambers.

The high-pressure chamber (HPC) cooling flow is reintegrated into the flow path at the third stage after cooling the HP chamber between the internal and external casings. The low-pressure chamber cooling flow is split into two streams after feeding the LP casing chambers; the larger stream is reintegrated into the exhaust section via properly dimensioned orifices while the remaining mass flow rate is directed toward the rear DGS. This stream is reinjected in the flow path via seal N° 5 after mixing with the rear DGS cooling flow. Finally, the remaining cooling flow in the balancing drum flows through seal n° 4 in the balancing chamber where it mixes with the front DGS cooling flow and reintegrates into the exhaust section.

Once the fluid network is designed, the heat transfer coefficients are computed using appropriate correlations and imposed, together with fluid bulk temperature, as boundary conditions for the thermal model. The temperature map of the expander is reported in Fig. 18. The effect of the balancing piston cooling flow is clear with a strong axial gradient between this region and the expander inlet. This cooling primarily aims at cooling the HP and LP casing chambers, which are around 450 °C, while as a positive side effect, it decreases the temperature of the rotor shielding the shaft-end region by the hot inlet temperature, and consequently reducing the cooling flow required by the front DGS. Indeed, the maximum allowable temperature of DGS of around 220 °C requires the design of a dedicated thermal management system, which consumes less than 0.5% of the total expander mass flow (considering the two DGSs) to counter both the significant internal viscous heat and the external heat transferred by conduction from the hot region of the expander.

The DGS cooling system has been designed in light of the findings proposed by the authors in another publication, in which a segregated conjugate heat transfer numerical procedure, suitable for DGS thermal design, has been presented and validated with experimental data provided by "FlowServe" with a rotating DGS test bench in sCO_2 environment [30]. The cooling system uses process gas at 160 °C to maintain the front seal at temperatures around 200 °C, while the rear one presents a slightly higher temperature due to the current secondary flow scheme. Indeed, the LP cooling flow, which is sCO_2 at 450 °C, warms up the rear external casing above the DGS, which is averagely hotter with respect to the front one. This heat is transferred to the seal via conduction, and consequently, a higher cooling mass flow rate is required with respect to the front DGS to limit the temperature to 220 °C.

Most of the cooling flow streams are reinjected into the machine after cooling the DGS, while a negligible part flows into the primary vent together with the buffer gas (pure CO_2). This mixture is recompressed and reintegrated back into the cycle. It is worth mentioning how the mixing between process and buffer gas alters the process gas composition, which shall be monitored and controlled during the cycle operations. The secondary vent is fed, instead, with a mixture of buffer (CO_2) and separation gas (air).

5.4 Rotordynamic Analysis. Lateral rotor-dynamic behavior for a flexible rotor and high energy density can be heavily affected by the stability of the vibration modes, especially the first forward mode in a "between bearings" rotor configuration. The practical way to estimate the margin for rotor instability is the logarithmic decrement (LogDec) of the nonsynchronous as given by the following equation:

$$\mathrm{LogDec} = \ln\left(\frac{Ae^{-\alpha\omega t_1}}{Ae^{-\alpha\omega(t_1+T_d)}}\right) = \alpha\omega T_d \tag{1}$$

The main factor that can affect the rotor stability are the 'Alford effect' and the 'seals effect'. The Alford effect is related to the additional torque introduced by the noncircumferential uniform pressure distribution along the expander stages. The seals' effect is related to the interaction between the fluid and rotor–stator surfaces, resulting in additional energy to precession whirling (typically the forward one) that could increase the lateral amplitude vibration. All those effects can be summarized on the LogDec stima; in case it is

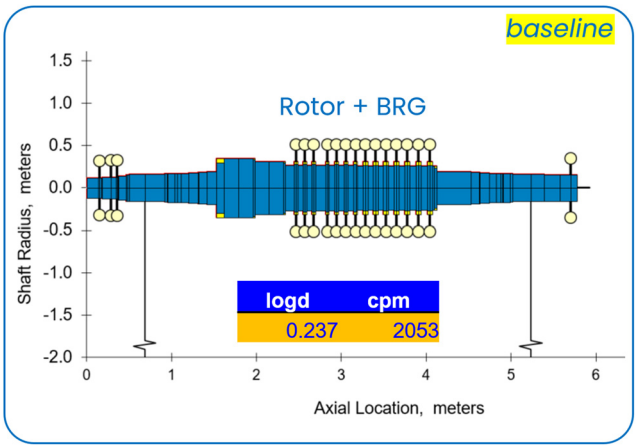

Fig. 19 Rotor + BRG rotordynamic model, Copyright 2023 by Baker Hughes Company—All rights reserved

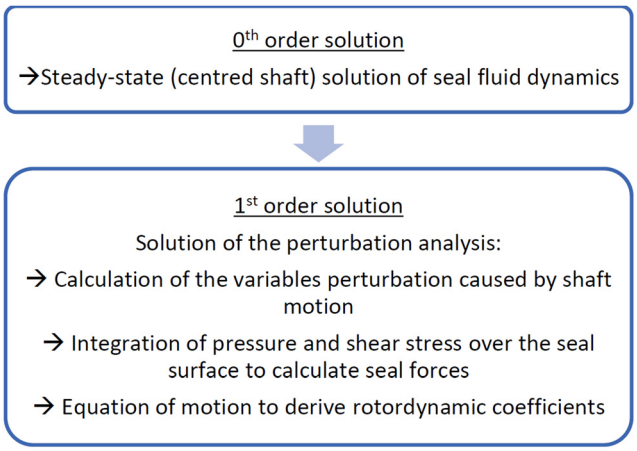

Fig. 20 SEALAB Bulk-flow modeling procedure, Copyright 2023 by Baker Hughes Company—All rights reserved

negative, the relevant mode vibration amplitude shall increase until nonlinearities effect is raised.

Dealing with a novel turbine design adds additional design challenges related to mechanical stability. The subsynchronous vibration, at the relevant frequency mode, is considered the most important contributor to the overall vibration. Once an instability effect is triggered, it cannot be controlled because the effects are related to the dynamic system itself (i.e., the position of the pole into the root locus). Usually, major modifications have to be considered to avoid high frequency instability such as changing clearances, rotor shape, designing additional dampers, modifying the geometry and type of seals, adding swirl breakers, and changing the type of bearings.

The starting point of the analysis is the rotor + bearing (BRG) stability check including the effect of the rotor-bearing interaction. The dynamic model configuration developed includes the rotor hot material properties, and minimum bearing clearances as shown in Fig. 19. From this point, the effects are added to the model as a constraint between the rotor and stator. This constraint is identified as the dynamic force coefficient. The Alford effect dynamic force coefficient is estimated according to API 612 8th edition using the following equation:

$$K_{xy} = -K_{yx} = \sum_{i=1}^{n} \left(\frac{HP \cdot B_t \cdot C}{D_t \cdot H_t \cdot N} \right)_i \tag{2}$$

where $B_t = 1.5$, and $C = 9.55$.

Seal dynamic effects are estimated using an in-house modeling tool called "SEALAB" which considers several geometrical details in terms of seals, rotor configuration, and thermodynamic fluid properties. Once the fluid dynamic steady-state equation (zeroth order) is solved (i.e., the steady-state distribution of pressure, fluid swirl ratio, and flow across the seals), a perturbation is applied in the equilibrium state. The linearized relationship between the rotor motion and the force is calculated as reported in Fig. 20 where the dynamic force coefficient is calculated.

Seals that are included in the SCARABEUS model are the inner casing seal, and balancing drum seals (inner and outer). The dynamic effect of the seals can be easily summarized by measuring the effective damping force coefficient as shown in the following equation:

$$C_{\text{eff}} = C_{xx} - \frac{K_{xy}}{\omega} \tag{3}$$

It is well known from the literature that the tangential force can act as a stabilizing or a destabilizing factor [13,37]. Damping acts as a stabilizing force that tends to reduce the rotor precession whirling, the opposite is the cross-coupling stiffness contribution as shown in Fig. 21.

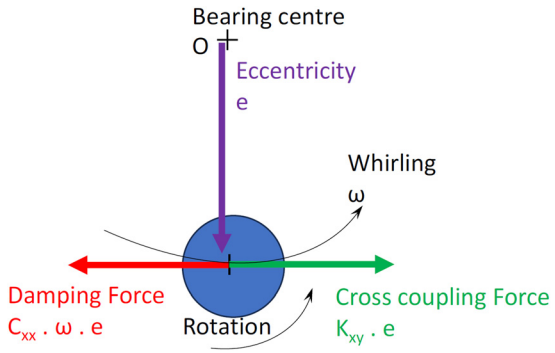

Fig. 21 Effective damping force schema Copyright, 2023 by Baker Hughes Company—All rights reserved

For a novel turbine design, the force dynamic coefficient estimation and the overall stability analysis can significantly affect the mechanical layout and rotor-dynamic verification. The dynamic behavior predictability is challenging for a rotor prone to mode instability, such as flexible rotors used for high density applications with high operational speed.

The effect of seals is dependent on some parameters such as; clearances, fluid thermodynamic properties across the seal, geometry (full labyrinth, half labyrinth, abradable), and preswirl, defined as the tangential fluid velocity component over the local rotor speed at the input side of the seal. Lower preswirl leads to a lower destabilizing effect acting on the rotor. The high value of the preswirl on the seal turns the C_{eff} highly negative producing a destabilizing effect on the first forward mode. In this case, a swirl brake device able to reduce initial preswirl on the seals can lead to a positive coefficient. Considering all the described destabilizing effects, the dynamic behavior of the rotor results in a stable condition as seen in Fig. 22.

5.5 Torsional Sizing. A preliminary torsional sizing can be conducted with rigid torsional considerations for the proposed expander rated for 130 MW, assuming a power factor of 0.85 that results in a synchronous generator sized for 153 MVA.

Based on data from electrical generators of a similar power rating, the rotor inertia (J_{gen}) of a 153 MVA, two-pole, electrical generator is estimated at around 4000 kg m^2. The rotor inertia of the expander (J_{exp}), for the proposed 14-stage, 620 mm hub diameter design is 320 kg m^2. An electrical malfunctioning torque (short circuit or out-of-phase synchronization) occurring at the generator air gap (M_{ag}), discarding possible amplifications generated by torsional resonances, results in a torque at the expander shaft end ($M_{\text{se exp}}$) given by

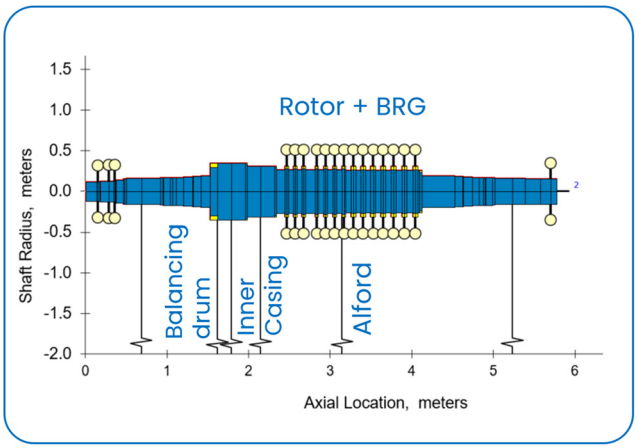

Fig. 22 Rotor + BRG in addition to all destabilizing effects included in the model, Copyright 2023 by Baker Hughes Company—All rights reserved

Eq. (4). With the inertia assumed for the generator, the torque at the expander shaft end is given by Eq. (5)

$$M_{\text{se exp}} = M_{\text{ag}}\left(\frac{J_{\text{exp}}}{J_{\text{exp}} + J_{\text{gen}}}\right) = M_{\text{ag}} J_{\text{ratio}}\left(\frac{1}{1 + J_{\text{ratio}}}\right) \tag{4}$$

$$M_{\text{se exp}} \cong 0.074\, M_{\text{ag}} \tag{5}$$

where $J_{\text{ratio}} = J_{\text{exp}}/J_{\text{gen}}$.

A conservative estimation for the electrical malfunctioning torque at the air gap can be obtained assuming a multiplication factor of 20 to the torque calculated with 153 MVA at 3000 RPM (314 rad/s). With this assumption, the peak torque to be withstood by the coupled end of the expander is 721 kNm

It can be seen that, in reason of the low J_{ratio}, the peak torque is only 1.74 times the normal torque (130 MW at 3000 rpm = 414 kN·m), which is an advantage when designing the shaft end of the expander. DGS requires an axial assembly and hence, if the shaft end of the expander is an integral piece of rotor, the diameter of the sleeves of the DGS needs to be greater than any other rotor diameter externally positioned with respect to the DGS. This assembly constraint, together with the fact that DGS are available only up to a certain size (approximately 350∼400 mm), establishes a maximum dimension for the coupled shaft end which limits the maximum torque with standable.

The inertia of the expander rotor is very small if compared to the generator rotor allowing an integral shaft end design with a tapered coupling (conicity 1/20) having a maximum diameter of 320 mm. The coupling hub, dimensioned with an outer diameter of 480 mm (1.5 times the internal maximum diameter) and having an axial length of 384 mm (1.2 times the internal maximum diameter), when assembled with 0.25% interference is suitable for a slippage torque capacity (calculated with a friction factor of 0.15) of around 1100 kNm, sufficiently higher than the 721 kNm estimated as peak torque in case of electrical fault. The DGS size finally selected has a diameter of 350 mm.

It is worth noting that the basic torsional sizing reported is impacted by the inertia of the expander rotor: a flow path designed at a larger diameter would have resulted in a larger J_{ratio}, resulting in the necessity to design a shaft end for a much larger torque. For example, with a J_{ratio}= 0.82 (consistent with the larger flow path analyzed: four stages on a 1280 mm hub diameter), the peak torque at the coupled shaft end would have been around 4400 kN·m. Even assuming a very large coupled shaft end (suitable to withstand this torque) which is connected to the rest of the rotor by means of Hirth or spline connections, a DGS of 350 mm limits the journal bearing size to around 320 mm: a peak torque of 4400 kN·m in the event of an electrical fault would result in 685 MPa of shear stress, which is an equivalent Von Mises stress of 1185 MPa. Such a huge equivalent stress would cause plastic deformation to the journal-bearing collar (which, in general, is not desirable) with essentially any possible material selectable for the rotor.

The lateral analysis, Sec. 5.2, has been executed with a coupling weight of 617 kg, consistent with a flexible coupling dimensioned for the peak torque capacity of 1100 kN·m deriving by the presented torsional sizing.

6 Conclusion

This paper has presented the aerodynamic-mechanical design and integration of a 14-stage 130 MW turbine operating with a CO_2/SO_2 mixture. The preliminary aerodynamic design was previously conducted using a mean line design model, in which the basic flow path design was obtained whilst considering various aerodynamic and mechanical constraints. The 3D blades were generated utilizing the mean line design results to initiate the steady-state numerical CFD simulations and predict the flow path aerodynamic performance.

Different exhaust cross-sections that satisfy all the necessary geometrical constraints were investigated and a final selection was made to minimize the aerodynamic losses. Steady-state simulations of the selected exhaust geometry reveal the design leads to a reduction of 0.34% in the total turbine power and a 2.08% drop in the power of the last stage. The calculated alternating stresses on the last rotor stage are found to be acceptable compared to the high cycle fatigue properties of nickel-based alloys. An unsteady, full annulus CFD simution of the last stage and the exhaust section was used to calculate the aerodynamic load fluctuations on the blade. The results showed a time average force magnitude that is 6.1% higher than the steady-state results. Frequency analysis revealed a stronger effect at a frequency that is 4 times the revolution frequency compared to responses at 42 and 47 times the revolution frequency; these three components are related to the number of outlet ports on the exhaust section and the number of rotor and stator blades, respectively. However, the forced excitations resulting from the number of blades showed larger amplitudes compared to the number of outlet ducts.

The design of various mechanical components were presented for the proposed turbine. The aerodynamic loads on the blades have been mechanically assessed and the results have shown that the mechanical design is safe. The rotor-dynamic behavior is also found to be acceptable with a sufficient stability margin when considering destabilizing effects (i.e., Alford and seal effects). The DGS are among the most critical components for the mechanical design of sCO_2 expanders. The installation of these seals is difficult due to the high pressure, high temperature, and high speed. These conditions lead to high thermal loads on the seals, which significantly complicates the design since the maximum temperature of the seals is limited to 220 °C. In this regard, a dedicated thermal management system has been designed. A cooling flow at 160 °C with a mass-flow rate of around 0.5% of the expander flow ensures proper cooling of the DGS regions. Moreover, the balancing drum cooling system is cooled using a cooling stream at 450 °C with a mass-flow rate of around 2.2% of the expander flow rate, which allows traditional stainless steel to be used for the high-pressure and low-pressure casing, avoiding the use of expensive Ni-based alloys for the heaviest components of the turbine.

Funding Data

- European Union's Horizon 2020 Research and Innovation Programme (Grant Agreement No. 814985; Funder ID: 10.13039/100010661).

Nomenclature

A = sinusoidal amplitude of the vibration
C_{eff} = effective damping coefficient
C_{in} = inlet absolute velocity (m/s)

C_{out} = outlet absolute velocity (m/s)
C_{xx} = damping force coefficient
D_t = ith stage bucket average pitch diameter (mm)
H_t = ith stage bucket average height (mm)
HP = the ith stage maximum delivered power (W)
J_{gen} = rotor inertia (kg m^2)
J_{exp} = rotor inertia of the expander (kg m^2)
$K.E$ = kinetic energy (kJ/kg)
K_{xy} , K_{yx} = dynamic force coefficients (kN/mm)
$\dot{m}$ = mass flow rate (kg/s)
M_{ag} = generator air gap malfunctioning torque (N·m)
$M_{se\ exp}$ = expander shaft end torque (N·m)
N = rotational speed (RPM)
NPF = nozzle passing frequency (Hz)
N_{R14} = number of blades in the 14th rotor
P = static pressure (bar)
P_0 = total pressure (bar)
s = specific entropy (J/kg K)
t_{blade} = time for one rotor blade pass (s)
t_1 = time of first max oscillation (s)
T_d = time period of the sinusoidal (s)
t_{rev} = time for one complete rotor revolution (s)

Greek Symbols

α = exponential rate of decay of the oscillation
Δ = difference
η_{tt} = total-to-total efficiency (%)
σ = maximum equivalent stress (MPa)
ω = pulsation frequency of the oscillation (Hz)

References

[1] White, M. T., Bianchi, G., Chai, L., Tassou, S. A., and Sayma, A. I., 2021, "Review of Supercritical CO_2 Technologies and Systems for Power Generation," Appl. Therm. Eng., **185**, p. 116447.
[2] Yin, J. M., Zheng, Q. Y., Peng, Z. R., and Zhang, X. R., 2020, "Review of Supercritical CO_2 Power Cycles Integrated With CSP," Int. J. Energy Res., **44**(3), pp. 1337–1369.
[3] Binotti, M., Marcoberardino, G. D., Iora, P., Invernizzi, C., and Manzolini, G., 2020, "Scarabeus: Supercritical Carbon Dioxide/Alternative Fluid Blends for Efficiency Upgrade of Solar Power Plants," Proceedings of AIP Conference Proceedings, AIP Publishing LLC, Daegu, South Korea, Oct. 1–4, p. 130002.
[4] Meng, F., Wang, E., Zhang, B., Zhang, F., and Zhao, C., 2019, "Thermo-Economic Analysis of Transcritical CO_2 Power Cycle and Comparison With Kalina Cycle and ORC for a Low-Temperature Heat Source," Energy Convers. Manage., **195**, pp. 1295–1308.
[5] Binotti, M., and Manzolini, G., 2019, "Supercritical Carbon Dioxide/Alternative Fluids Blends for Efficiency Upgrade of Solar Power Plant," Proceedings of Third European Supercritical CO_2 Conference, Paris, France, Deu, Sept. 19–20, pp. 141–149.
[6] Morosini, E., Ayub, A., di Marcoberardino, G., Invernizzi, C. M., Iora, P., and Manzolini, G., 2022, "Adoption of the CO_2+ SO_2 Mixture as Working Fluid for Transcritical Cycles: A Thermodynamic Assessment With Optimized Equation of State," Energy Convers. Manage., **255**, p. 115263.
[7] Crespi, F., de Arriba, P. R., Sánchez, D., and Muñoz, A., 2022, "Preliminary Investigation on the Adoption of CO_2-SO_2 Working Mixtures in a Transcritical Recompression Cycle," Appl. Therm. Eng., **211**, p. 118384.
[8] Zhang, H., Zhao, H., Deng, Q., and Feng, Z., 2015, "Aerothermodynamic Design and Numerical Investigation of Supercritical Carbon Dioxide Turbine," ASME Paper No. GT2015-42619.
[9] Shi, D., Zhang, L., Xie, Y., and Zhang, D., 2019, "Aerodynamic Design and Off-Design Performance Analysis of a Multi-Stage S-CO_2 Axial Turbine Based on Solar Power Generation System," Appl. Sci., **9**(4), p. 714.
[10] Bidkar, R. A., Mann, A., Singh, R., Sevincer, E., Cich, S., Day, M., Kulhanek, C. D., Thatte, A. M., Peter, A. M., Hofer, D., and Moore, J., 2016, "Conceptual Designs of 50 MWe and 450 MWe Supercritical CO_2 Turbomachinery Trains for Power Generation From Coal. Part 1: Cycle and Turbine," The 5th International Symposium - Supercritical CO2 Power Cycles, San Antonio, TX, Mar. 28–31.
[11] Kim, W. J., and Song, S. J., 2003, "Rotordynamic Forces Due to Rotor Sealing Gap in Axial Turbines," ASME Paper No. GT2003-38616.
[12] Uysal, S. C., White, C. W., Weiland, N., and Liese, E. A., 2022, "Cooling Analysis of an Axial Turbine for a Direct Fired sCO_2 Cycle and Impacts of Turbine Cooling on Cycle Performance," Energy Convers. Manage., **263**, p. 115701.
[13] Ehrich, F. F., 1999, "Chapter 1: Vibration Considerations in the Design of Rotating Machinery," *Handbook of Rotordynamics*, Kriegar Publishing Company, Malabar, FL.
[14] Salah, S. I., Khader, M. A., White, M. T., and Sayma, A. I., 2020, "Mean-Line Design of a Supercritical CO_2 Micro Axial Turbine," Appl. Sci., **10**(15), p. 5069.
[15] Fu, J., Liu, J., and Zhou, S., 2007, "Experimental and Numerical Investigation of Interaction Between Turbine Stage and Exhaust Hood," J. Power Energy, **221**(7), pp. 991–999.
[16] George, T. J., Shen, M.-H. H., Scott-Emuakpor, O., Nicholas, T., Cross, C. J., and Calcaterra, J., 2005, "Goodman Diagram Via Vibration-Based Fatigue Testing," ASME J. Eng. Mater. Technol., **127**(1), pp. 58–64.
[17] Kalra, C., Hofer, D., Sevincer, E., Moore, J., and Brun, K., 2014, "Development of High Efficiency Hot Gas Turbo-Expander for Optimized CSP Supercritical CO_2 Power Block Operation," Proceedings of the Fourth International Symposium—Supercritical CO_2 Power Cycles (sCO_2), Pittsburgh, PA, Sept. 9–10, pp. 1–11.
[18] Wilkes, J., Robinson, K., Wygant, K., Pelton, R., and Bygrave, J., 2022, "Design and Testing of a 275 Bar 700 Degree Celsius Expander for an Integrally Geared Supercritical CO_2 Compander," ASME Paper No. GT2022-83284.
[19] Guédez, R., Barberis, S., Maccarini, S., López-Román, A., Milani, A., Pesatori, E., Oyarzábal, U., and Sánchez, A., 2022, "Design of a 2 MW Molten Salt Driven Supercritical CO_2 Cycle and Turbomachinery for the SOLARSCO2OL Demonstration Project," ASME Paper No. GT2022-82013.
[20] Stein, P., Pfoster, C., Sell, M., Galpin, P., and Hansen, T., 2016, "CFD Modeling of Low Pressure Steam Turbine Radial Diffuser Flow by Using a Novel Multiple Mixing Plane Based Coupling: Simulation and Validation," ASME Paper No. GTP-15-1332.
[21] Živný, A., Macálka, A., Hoznedl, M., Sedlák, K., Hajšman, M., and Kolovratník, M., 2017, "Numerical Investigation and Validation of the 1090 MW Steam Turbine Exhaust Hood Flow Field," ASME Paper No. GT2017-63576.
[22] Fu, J.-L., Liu, J.-J., and Zhou, S.-J., 2012, "Unsteady Interactions Between Axial Turbine and Nonaxisymmetric Exhaust Hood Under Different Operational Conditions," ASME J. Turbomach., **134**(4), p. 041002.
[23] Salah, S. I., Crespi, F., White, M. T., Muñoz, A., Paggini, A., Ruggiero, M., Sánchez, D., and Sayma, A. I., 2023, "Axial Turbine Flow Path Design for Concentrated Solar Power Plants Operating With CO_2 Blends," Appl. Therm. Eng., **230**, p. 120612.
[24] Kim, H. S., Cho, M., and Song, S. J., 2003, "Stability Analysis of a Turbine Rotor System With Alford Forces," J. Sound Vib., **260**(1), pp. 167–182.
[25] Oleksak, R. P., and Rouillard, F., 2020, "4.14 - Materials Performance in CO_2 and Supercritical CO_2," *Comprehensive Nuclear Materials*, 2nd ed., R. J. M. Konings, and R. E. Stoller, eds., Elsevier, Oxford, pp. 422–451.
[26] European Commission, 2021, "Desolination: Demonstration of Concentrated Solar Power Coupled With Advanced Desalination System in the Gulf Region," European Union H2020 Project.
[27] Liao, X., Chalumeau, S., Crespi, F., Prieto, C., Lopez-Roman, A., Rodriguez de Arriba, P., Martínez, N., Sánchez, D., Paggini, A., and David, P., 2022, "Life Cycle Assessment of Innovative Concentrated Solar Power Plants Using Supercritical Carbon Dioxide Mixtures," ASME Paper No. GT2022-83576.
[28] Bidkar, R. A., Sevincer, E., Wang, J., Thatte, A. M., Mann, A., Peter, M., Musgrove, G., Allison, T., and Moore, J., 2017, "Low-Leakage Shaft-End Seals for Utility-Scale Supercritical CO_2 Turboexpanders," ASME J. Eng. Gas Turbines Power, **139**(2), p. 022503.
[29] Rafanelli, I., Generini, G., Andreini, A., Diurno, T., Girezzi, G., and Paggini, A., 2023, "Development and Validation of a Segregated Conjugate Heat Transfer Procedure on a SCO_2 Dry Gas Seal Test Bench," ASME Paper No. GT2023-101987.
[30] Steinmann, D., Kassimi, R., Kleiner, J., Susini, P., Milani, A., and Dozzini, M., 2022, "Dry Gas Seals Design for Centrifugal Compressors in Supercritical CO_2 Application," Seventh International sCO_2 Power Cycles Symposium, San Antonio, TX, Feb. 21–24, Paper No. 187.
[31] Abdeldayem, A., White, M. T., and Sayma, A. I., 2021, "Comparison of CFD Predictions of Supercritical Carbon Dioxide Axial Flow Turbines Using a Number of Turbulence Models," ASME Paper No. GT2021-58883.
[32] Jang, H. J., Kang, S. Y., Lee, J. J., Kim, T. S., and Park, S. J., 2015, "Performance Analysis of a Multi-Stage Ultra-Supercritical Steam Turbine Using Computational Fluid Dynamics," Appl. Therm. Eng., **87**, pp. 352–361.
[33] Aqel, O., White, M., and Sayma, A., 2021, "Binary Interaction Uncertainty in the Optimisation of a Transcritical Cycle: Consequences on Cycle and Turbine Design," Proceedings of Fourth European sCO_2 Conference for Energy Systems, Virtual Online, Mar. 23–24, pp. 164–176.
[34] Dubiez-Le Goff, S., Couturier, R., Guétaz, L., and Burlet, H., 2004, "Effect of the Microstructure on the Creep Behavior of PM Udimet 720 Superalloy—Experiments and Modeling," Mater. Sci. Eng. A, **387–389**, pp. 599–603.
[35] Abdeldayem, A., White, M., Paggini, A., Ruggiero, M., and Sayma, A. I., 2022, "Integrated Aerodynamic and Structural Blade Shape Optimisation of Axial Turbines Operating With Supercritical Carbon Dioxide Blended With Dopants," ASME J. Eng. Gas Turbines Power, **144**(10), p. 101016.
[36] Salah, S. I., White, M. T., and Sayma, A. I., 2022, "A Comparison of Axial Turbine Loss Models for Air, sCO_2 and ORC Turbines Across a Range of Scales," Int. J. Thermofluids, **15**, p. 100156.
[37] Vance, J. M., Zeidan, F. Y., and Murphy, B. G., 2010, Machinery Vibration and Rotordynamics, John Wiley & Sons, Chapter No. 6, Chichester, UK.